Summer 8-8-2024

UAS-Enhanced Rock Mass Characterization of the Left Abutment at Madison Dam, Ennis Montana

Karl Farber

UAS-Enhanced Rock Mass Characterization of the Left Abutment at Madison Dam, Ennis Montana

by

Karl Farber

A non-thesis report submitted in partial fulfillment of the requirements for the degree of

Master of Science in Geoscience, Engineering Geology Option

Montana Tech

2024

Abstract

Recently, advancements in drone technology for mapping rock mass features have been on the rise and are becoming more of a staple for geotechnical site investigation. The safety of humans when collecting field data is a top priority and using drones, or unmanned aerial systems (UAS), can minimize those safety risks. Creating models that depict accurate data of rock mass discontinuities and possible failure modes in inaccessible areas has its challenges, but drones can provide a way of addressing those challenges.

This study involves using UAS-based data collection to capture rock mass fractures at Madison Dam just North of Ennis, Montana. A manual flight capturing video data and three autonomous flights capturing photos were performed on-site on December 7, 2023. In the autonomous flights, the camera was pointed primarily vertically downward. During the manual flight, the camera was directed toward the steeply inclined rock face, in a more horizontal orientation. Both methods of data collection provided data for a complete point cloud model using a photogrammetry software package called Pix4DMapper.

In addition to the modeling, a series of rock characterization and analysis was performed using samples from the field and joint set data collected from the drone imagery. Testing included a multistage triaxial test to determine the shear strength of the intact rock, as well as a series of kinematic analyses generating possible failure modes of the rock mass. The results from this study indicate that the rock at Madison Dam is highly fractured and has a possibility of failure.

Introducing drone photogrammetry can be time efficient and pose much safer human conditions for creating real-time data from the field. Although there are challenges when collecting drone imagery data, it can give helpful data to the engineering community when needing data from places that are dangerous for human access.

Acknowledgements

Table of Contents

List of Figures

1. Introduction

Characterizing rock mass discontinuities and strength parameters is important for geotechnical engineering design. Some sites allow for human data collection with low safety risks and other sites require an alternative solution when collecting data. Photogrammetry is a tool that can produce three-dimensional models of sites from remotely collected imagery, allowing for analyses to be performed in a way that is more time-efficient and safer than the traditional methods. Unmanned aerial vehicles known as drones are now commonly used to capture data from larger areas that may take more time to collect without remote sensing. This is especially encouraged if there is a risk of human injury when data collection is being performed.

In this project, a drone was utilized to collect photogrammetric data of a near-vertical rock mass present in the left abutment of the Madison Dam, located near Ennis, Montana. The project goals were to perform data collection using a drone, apply photogrammetric techniques to the imagery to develop an accurate 3D point cloud model of the rock mass discontinuities, and conduct kinematic and finite element engineering analyses. To provide shear strength parameters for the analysis, rock samples were collected from the site and subjected to tilt tests and a multistage triaxial test.

The ability to use UAS in geotechnical modeling is a recently new technique. Although this is often considered the safest and most efficient way to collect data, it can have its drawbacks. One primary drawback is that it may be challenging to collect photos at the correct orientations for the most accurate model. This method of data collection has improved drastically in the past 10 years, due to advancements in digital camera technology, having the ability to get to places where humans can’t, and to improve the efficiency during projects (Niedzielski, 2018). With proper planning and execution using this method is advantageous for mapping and modeling in areas where direct access by humans is difficult.

2. Research Project

The objectives for this research are to utilize UAVs to collect imagery for field mapping via photogrammetric 3D models and to perform engineering analyses of the rock mass. The overall goal is to ensure the safety of the people working on Madison Dam. The photogrammetric models are designed to show the major discontinuities (rock joints) within the rock mass. By creating models to show joints in the rock mass, failure modes can be identified and recorded for further investigation and analysis, and eventual design of mitigation alternatives. Appendix A shows a flow chart of the steps taken to complete this research project.

2.1. Research Site: Madison Dam

The project site is located just north of Ennis, Montana. The structure at the site is a concrete gravity dam. The dam was built in 1906 in a very narrow portion of the Madison River. To the North, the river flows through the steep Bear Trap canyon before it joins the Jefferson and Gallatin rivers, eventually forming the Missouri River (Pinckney, 1980). Upstream of the dam towards Ennis, the steep canyon transitions into a broad valley bordered by the Madison and Gravelly Mountain ranges.

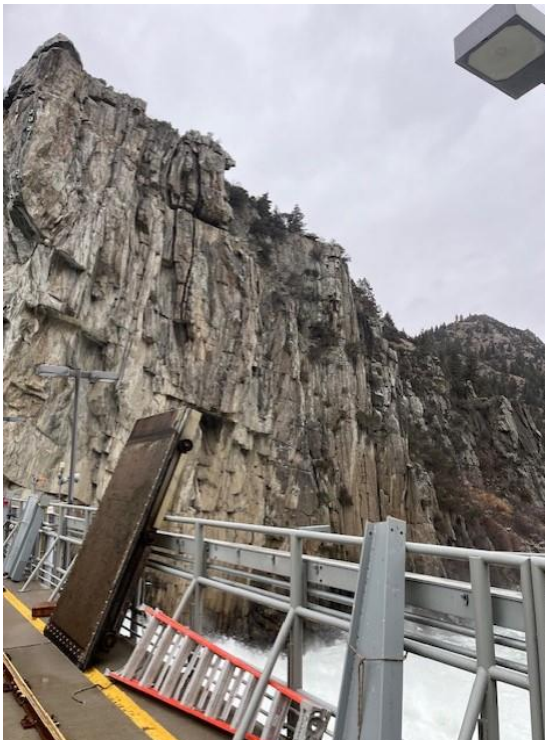

Figure 1: Left abutment rock mass downstream of Madison Dam

Madison Dam is a hydroelectric dam owned and operated by Northwest Energy. The dam spans 257 feet wide and is about 40 feet tall. It is one of eleven operating hydroelectric dams in Montana and has a generating capacity of nine megawatts

of power (www.Northwesternenergy.com). Data collection at the site was focused on the left abutment where a near vertical rock mass is located. Figure 1 shows an image of the left abutment. This rock mass is very fractured and shows signs of possible failure in some locations. The rock mass at the site is part of a ridge that trends northwesterly and is part of an extension of the Madison Range (Pinckney, 1980).

2.2. Site Geology

As shown in Figure 2, the rock found at the project site is a high-grade metamorphic gneiss. The gneiss consists of medium-sized grains and is well-foliated and banded. The bands, evident in Figure 3, contain alternating layers of light and darker-colored minerals. The light-colored bands, or leucosomes, are comprised of plagioclase, quartz, biotite, and small amounts of potassium feldspar and garnet. The dark-colored bands are melasomes, comprised of biotite, hornblende, plagioclase, quartz, and small amounts of garnet (Pinckney, 1980). High-grade metamorphic rock masses commonly contain closely spaced, steeply inclined joints parallel to foliations (Goodman, 1993). The rock at this site experiences a wet environment due to the spraying water from the dam, and snowmelt and rainy seasons in late spring and early summer. These conditions can increase the erosion rates and can reduce the strength of the joint surfaces.

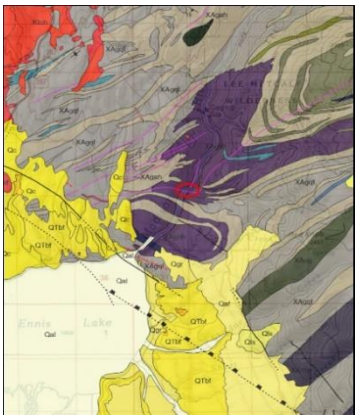

Figure 2: Geologic map of study area (red circle) dark purple shade represents the Gneiss unit found at the site (Ngmdb.usgs.gov)

Figure 3: Prepared 2” diameter samples with both leucosome (light) and melasome (dark) layering

2.3. Previous Study

A geotechnical report prepared by NTL/Terracon documented geotechnical rock slope stability design and construction observations on the left abutment area of Madison Dam (NTL/Terracon 2011). This work was performed due to a rockfall incident that occurred on August 30, 2010. The study focused on the upstream rock face along the left abutment. A block of the rock mass estimated to be 400,000 pounds fell, destroying the two bays of the dam's left abutment superstructure. NTL/Terracon started with a reconnaissance of the exposed and cracked block in the rock mass, including viewing the rock mass by helicopter and repelling from the top using rock climbing equipment for closer inspection. After this initial site investigation was performed, the design for this rock slope mitigation included a set of twelve, No. 20 (2.5" diameter) Grade 75 All-Thread bars. The bars were 30 feet in length in order to provide conservative embedment into the critical rock behind the fracture. The bolt pattern was designed to provide a coupled resistance to the moment that would be induced by any toppling blocks if the bolts were to fail. To further insure rockfall protection for people working at the site a Geobrugg ring net and high-strength steel mesh were installed (NTL/Terracon 2011). The high-strength steel mesh and the No 20 rock bolts along with the rock mass discontinuities can be seen in the 3d models produced using drone photogrammetry. Figures 4 and 5 are photos of the upstream face of the left abutment rock mass.

Figure 4: Photo taken of the cracked block by NTL/Terracon employee in 2010 (NTL/Terracon 2011).

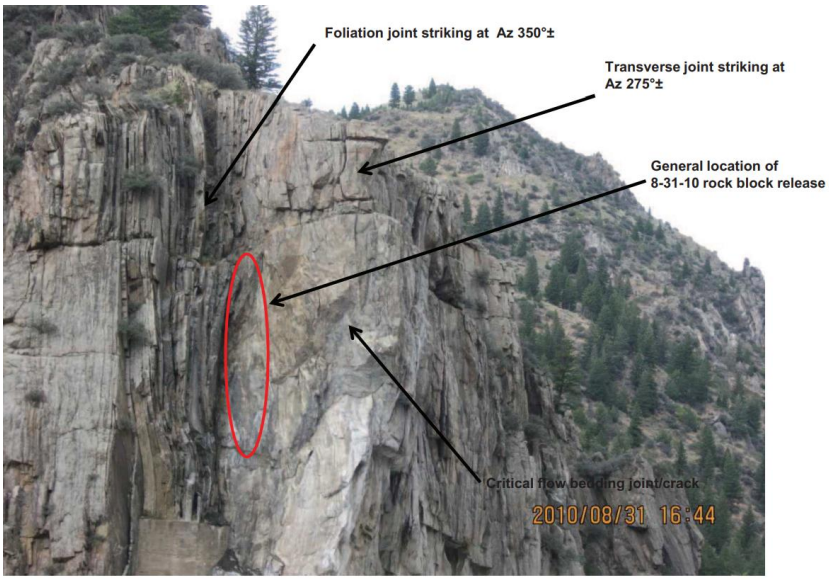

Figure 5: Photo taken by NTL/Terracon employee in 2010 showing the location of the block release and joint strike measurements (NTL/Terracon 2011).

3. Site Characterization

When characterizing the left abutment at Madison Dam the main area of concern for this project is the downstream portion of the rock mass. To create a 3D model of the downstream rock mass multiple missions were executed to capture optimal imagery data. Once all the data were collected at the site, including rock samples, further investigations were performed to determine critical zones and rock strength.

3.1. UAV-Based Imagery Collection

Data collection was performed using a drone to capture both video and autonomous photos. Photogrammetry can be performed on both types of datasets to produce a point cloud and a 3D surface/mesh which shows geologic structures (joints). A Parrot Anafi USA drone (shown in Figure 6) owned by Northwestern Energy was used to collect the videos and images (www.parrot.com). This platform is a USA drone product and contains a 4K camera (Figure 7) with both wide angle/zoom settings, also including a thermographic setting that was not used for this study. Due to this site being regulated by the Federal Energy Regulatory Commission (FERC) a drone built and produced in the United States is required (Dams in Montana, 2018).

Figure 6: Parrot ANAFI USA drone platform (www.parrot.com)

Figure 7: Detailed images of camera found on the Parrot ANAFI (www.parrot.com)

The autonomous missions were planned using Pix4D Capture Pro. This software enables the drone to capture images at a certain overlap to collect data for a

point cloud; a 90 % overlap was used for the autonomous photo flights. The missions consisted of double-grid flying patterns to increase the amount of images collected. Figure 8 shows a photo taken just before initiating one of the three autonomous flights. The video imagery dataset was collected by flying the drone manually, moving horizontally back and forth or parallel with the rock face at the site. The camera settings can be adjusted for different video shots and different camera modes can be selected on the tablet before or during flights.. For the manual flight on site, the “cinema camera” mode was utilized. This option keeps the camera stable while the drone is moving in the air, creating better video footage for the photogrammetry software to process. After flying, still images from the video were screen captured to use in the modeling software.

Collecting drone imagery can be challenging, as there are many variables that can affect the quality of the data being collected. These can include:

1. bad weather (wind, rain etc.)
2. shadows from different sun angles
3. snow or water on the rock surface, which can reflect light and distort the model
4. technical difficulties when connecting the drone with the controller

When at the site on December 7, 2023, the weather started out a bit rainy and windy. Fortunately, rain and wind cleared around 10:30 am leaving an overcast cloudy day. This type of weather is preferred for photogrammetry due to minimizing shadows from trees and rock that can potentially create holes in the 3D model.

Figure 8: Starting an autonomous flight on-site with Northwest Energy employee Brian Kremer

3.2. Point Cloud Modeling Process

Pix4D mapper was employed to create models of the site using the photogrammetric data collected in the field. This image processing software automatically finds thousands of common points between images and ties them together using a methodology called “structure from motion” (SfM) (support.pix4d.com). Pix4D mapper is a very user-friendly software that is fast and produces quality models. When running the software there are three processing steps:

1. Initial Processing
2. Point Cloud Mesh
3. DSM, Ortho-mosaic and Index

The initial processing step involves identifying key-points in the images. Key-points are generated by identifying specific features in the images that are the same or closely match.

During this step, the internal focal length and external parameters of the camera are calibrated. Step two creates a point cloud mesh using point densification: additional tie points are created based on automatic tie points, resulting in a densified point cloud. For this study, manual tie points were also inserted. Manual tie points are generated by finding easy to identify objects within the point cloud to then re-optimize the images with a specific focus on that object. This makes it easier for the textured mesh in the final step to fill in any holes. Based on the densified point cloud, a 3D textured mesh can be created. The final step enables the creation of a digital surface model (DSM). The DSM fills in any holes or "noise" in the point cloud to match the color and structure of the 3D model (Support.pix4d.com). This enables the computation of volumes and generation of orthomosaics.

3.3. Photogrammetric Modeling Results

Pix4D Mapper was used to construct the photogrammetric models of Madison Dam. After performing the three processing stages, a quality report is generated. The quality report is automatically displayed after each step of processing. The report consists of several sections describing the model being produced, including a quality check displaying information about the number of key points produced per image, the calibration of the dataset, camera optimization, matching, point cloud density, absolute geolocation variance, and georeferencing. The quality report also includes the root mean squared (RMS) error (Pix4Dmapper Quality report, 2024). RMS error is a local indicator of how well Pix4D fits the model to the ground control points (GCPs). Since there were no GCPs on site, manual tie points were inserted into the point cloud model. Once the manual GCPs were inserted, the model was run again using the re-optimization tool. This recalibrates the point cloud data to locate the manual tie point placed in the model.

Different procedures were followed when constructing the 3D models from the two types of imagery. The nadir (vertical downward) autonomous flight data was very straightforward to

process in Pix4D Mapper. The point cloud produced from the three autonomous flights created a high-quality point cloud for the flatter portion of the site above the rock mass, but due to spraying water from the dam showed large holes on the face of the cliff area. This was due to the camera angle and the near vertical orientation of the rock mass being almost parallel with each other. Figure 9 shows the autonomous flight 3D model. Another drawback to the nadir autonomous flight was that it had trouble capturing imagery of the near-vertical rock face. The manual flight was done to get camera angles that captured the face of the rock mass without the interference of spraying water from the dam. This flight captured video data, and the process of producing a model was a bit more challenging. In order to capture still frames from the video, screen captures were taken about every 3 seconds. This gave the image processing software enough image overlap to produce a 3D point cloud, although there was quite a bit of noise surrounding the model due to some of the images not being entirely focused on the rock mass face. Figure 10 shows the pixels with noise scattered around the model.

Figure 9: Autonomous flight model produced in Pix4D Mapper

Figure 10: Manual flight model produced in Pix4DMapper

Overall, the quality of both models was judged to be adequate. Since the images in the autonomous model were georeferenced, an RMS value could be produced. The georeferenced images are oriented using latitude and longitude locations from where the drone was located when capturing the image; still frames extracted from the video do not contain this metadata, so the model produced from the manual flight was not georeferenced. The quality report produced from Pix 4D Mapper shows an RMS error of about 0.80 to 1.20 feet for the autonomous model. Appendix A contains the full quality report produced by Pix 4D Mapper.

4. Rock Mass Characterization

For this study, the characterization of the rock mass included three components: a multistage triaxial test for determining the shear strength of the intact rock, tilt test trials for evaluating the external friction angle along the joint surfaces, and the orientations of the joint sets in the rock mass were identified in order to predict rock mass failure modes with a kinematic analysis. Each component delivered important data that helped to determine how the rock mass might behave in its current state.

4.1. Multistage Triaxial Test for Shear Strength of Intact Rock

When characterizing a rock mass, determining the shear strength of the intact rock can be difficult. Ideally, a suite of triaxial tests is performed with at least three specimens to obtain a failure envelope. However, when samples are difficult to obtain, a single multistage triaxial test can provide the required data needed for a failure envelope. One multistage triaxial test was performed for this project using the TerraTek servo-controlled hydraulic load frame shown in Figure 12. The maximum force the load frame can apply is 330,000 lbs, and the maximum confining pressure that this frame can produce is 20,000 psi. The multistage triaxial test (Kim and Ko, 1979) involves applying load to the specimen in three different stages. In the first two stages, the sample is loaded to its volumetric strain inflection point. It is assumed that the inflection point corresponds to a stress level that is close to the peak stress but has not caused significant damage. Determining this point can be difficult, which makes the multistage triaxial test challenging to perform. During the last stage of the test, the specimen is brought to failure.

Multiple specimens were cored from samples gathered from the site. Coring the specimens from the field was difficult due to the banding and foliation of the rock. Some layers were weaker than others causing the rock to break during the coring process. Once coring was complete, three specimens were cut and ground to the correct shape and flatness parameters for

testing, but only one specimen was judged to be suitable. The specimen that was used for testing was cored parallel with the banding. The specimen parallel with the banding was selected because it had the least visible discontinuities and was the longest of the three specimens. Figure 11 shows the specimen prior to the testing.

Conducting the multistage triaxial test included the following steps:

1. Measure the mass, length, and diameter of the specimen and enter the values into the testing software.
2. Wrap the specimen in a plastic heat shrink material and seal both ends so there is no risk of confining pressure oil penetrating the sample.
3. Attach the axial LDVTs and radial strain device to the sample to allow the displacement measurements to be recorded.
4. Connect all of the sensors to the testing machine and raise the specimen into the testing chamber.
5. Once in the chamber oil is pumped around the sample to apply confining pressure. In this case, confining pressures for the three stages were 500, 1000, and 1500 psi.
6. The axial loading ram is lowered to contact the specimen.
7. Start the test and apply axial stress to the specimen.
8. Bring the specimen to the volumetric strain inflection point for the first two stages.
9. Finally, bring the specimen to failure to measure the actual peak stress corresponding to the highest confining pressure.

Once the multistage test was completed, both the axial stress vs. axial strain and the axial stress vs. volumetric strain curves were used for a Mohr-Coulomb failure envelope. The Mohr-Coulomb strength parameters produced by the failure envelope are the friction angle (angle of the line of best fit) and cohesion (y-intercept value)

Figure 11: Specimen used for the multistage triaxial test cored parallel with the bedding planes.

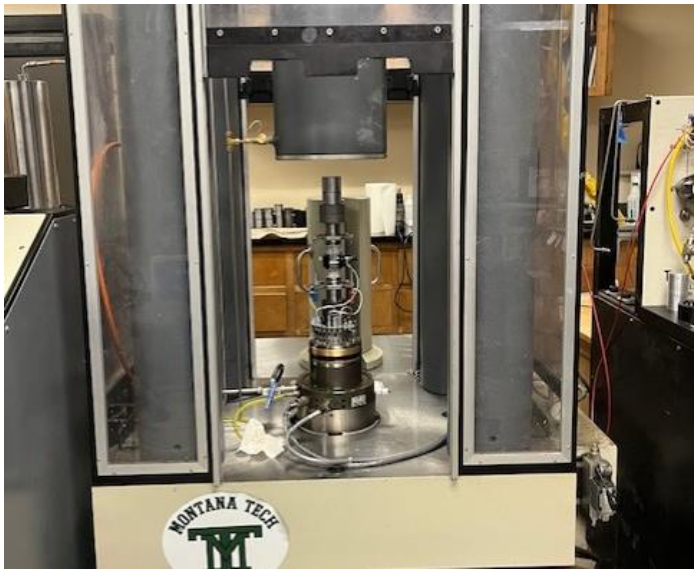

Figure 12: The load frame with the specimen in a wrapped membrane so no oil can penetrate the specimen

While performing the multistage test on the specimen, two different lines were analyzed on the graph. The first was the axial stress vs. volumetric strain, which helped to determine the inflection points of the specimen. The second set of data was the axial stress vs. axial strain curve. This produced peak stress data for the specimen. Figure 13 shows a graph representing the multistage triaxial test data. This includes both inflection points, the peak strength, and the axial stress values used for the Mohr-Coulomb failure envelope.

Once all three stages were complete, the peak stresses and corresponding confining pressure values were input into Rocscience software, RocLab that uses the data generated from the multistage triaxial test to construct a Mohr-Coulomb failure envelope. This method determines the specimen's peak cohesion and internal friction angle by first plotting Mohr's circles using confining pressure (sigma 3) and axial stress at the inflection point or peak stress (sigma 1), then fitting a line (failure envelope) tangent to the circles. Figure 14 shows Mohr's circles generated in RocLab Rocscience Software. This rock was very strong, producing an

internal friction angle of 57 degrees and a peak cohesion of 3800 psi. Table 1 summarizes the confining pressures and the corresponding peak strength values.

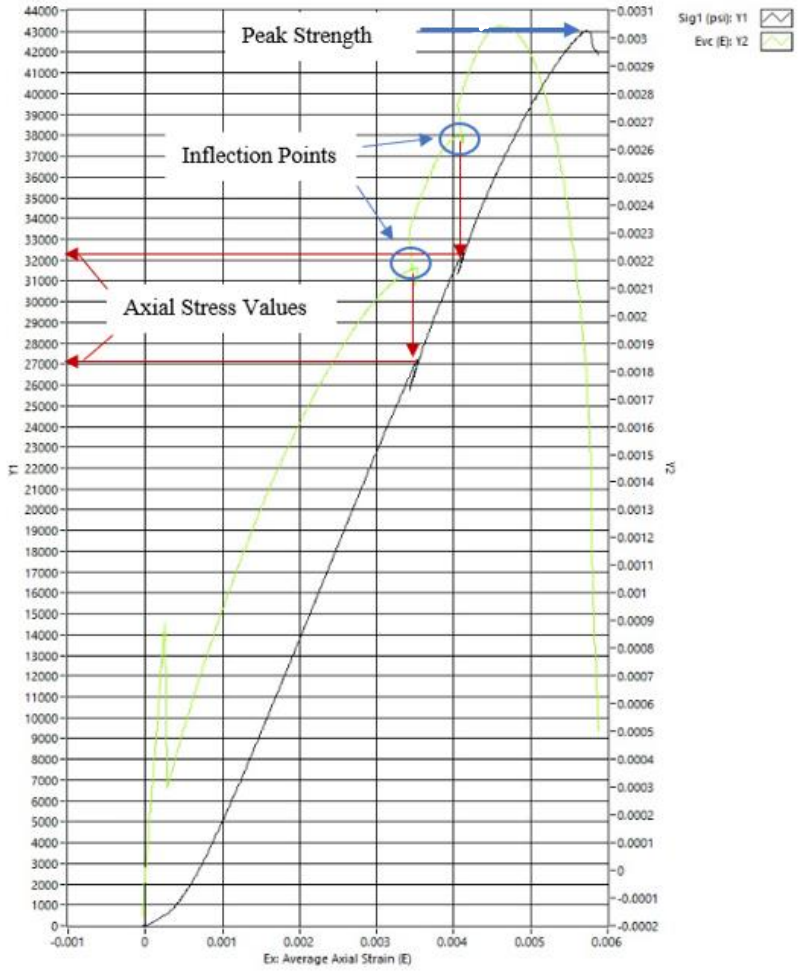

Figure 13: Multistage triaxial test data graph. Axial stress (left-side y axis) and volumetric strain (right side) are plotted vs. axial strain. The volumetric strain inflection points (blue circles) are used to define the peak axial stresses for the first two stages (red arrows); the peak strength is used as the third point in the Mohr-Coulomb analysis.

Table 1: Shear strength data and Mohr-Coulomb failure envelope results from multistage triaxial test

Confining pressures (psi)	Axial Strength Values (psi)	Cohesion (psi)	Friction Angle
500	27200	3800	57°
1000	32300		
1500	43000		

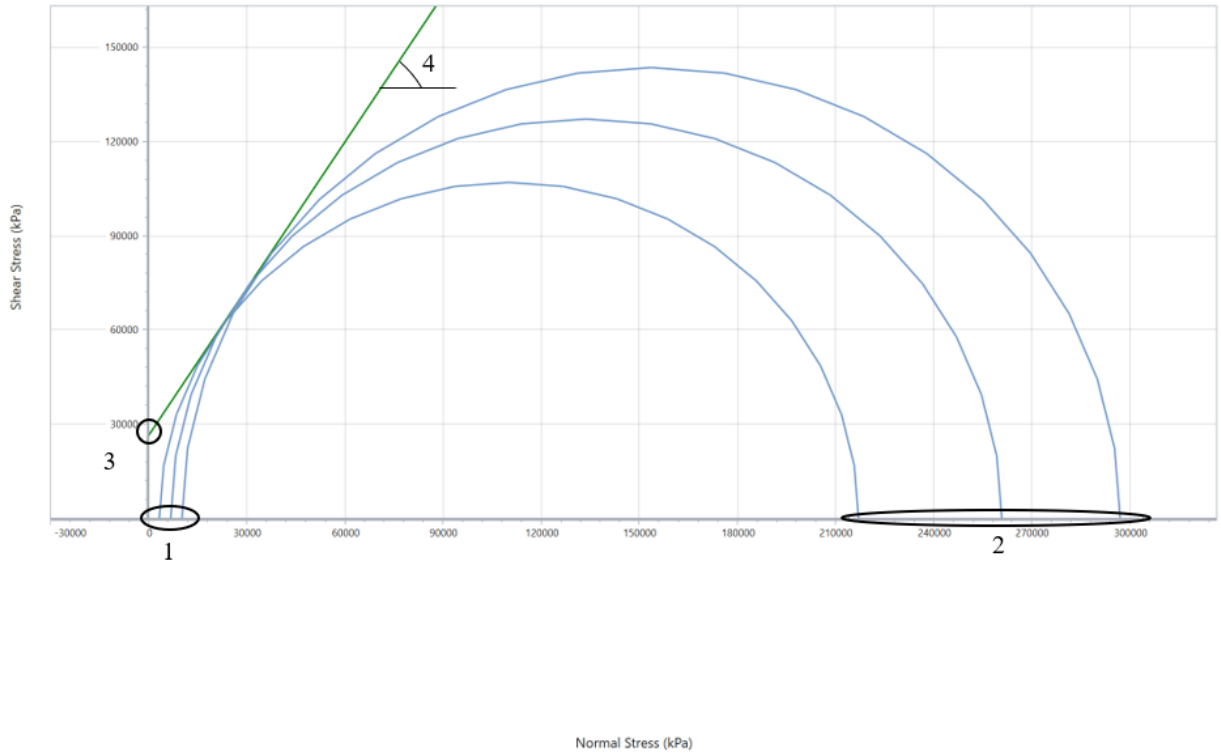

Figure 14: Mohr's circles (blue) representing data from multistage test. The green line shows the best fit failure envelope. (1) sigma 3 confining pressures, (2) sigma 1 corresponding to inflection points from stages 1 and 2, and peak shear stress from stage 3. (3) peak cohesion at the y-intercept, (4) internal friction angle in degrees

4.2. Tilt Test for Friction Angle of Joint Surfaces

The kinematic analysis is often combined with a rough stability analysis that requires an estimate of the ("external") friction angle of the rock joint surfaces. The tilt test is used to measure the joint friction angle. This simple test is performed by laying one sample of rock on top of another sample, and tilting the two samples until the top rock slides off the bottom rock. Once the top rock slips, the angle of the bottom sliding surface with respect to the horizontal is recorded. Figure 15 shows the tilt test being performed. Tilt tests were performed using smaller samples collected from the site. This test was repeated fifty times giving an average "external" joint friction angle of 29 degrees. Appendix B contains the full set of results from the fifty trials.

Figure 15: Tilt test machine with two hand samples from the Madison Dam rock mass

4.3. Rock Joint Set Orientations

The orientations of the joint sets in the rock mass are needed to perform a kinematic analysis, which is concerned with the movement direction of the rock blocks and provides potential failure modes. Using the 3D point cloud of the site provided by Pix4D Mapper, Cloudcompare can be utilized for measuring discontinuity orientations. Cloudcompare is a free open-source software that has the ability to calculate dip and dip directions of joints using point cloud data. In this case, five joint sets were identified within the 3D model, corresponding to the different colored lines shown in Figure 16. Once joint data were collected in Cloudcompare, they were uploaded into Rocscience's Dips program. Dips is a stereographic projection software designed for interactive analysis of orientation-based geological data. In this software, the user can define sets of rock mass orientations, and the mean dip and dip direction angles are calculated automatically. Figure 17 shows the Dips stereonet plot of the five joint sets with the poles of the dip and dip directions as black squares. Table 2 summarizes the average dip and dip direction of the five joint sets and the different colors associated with each joint set. Dips can also be used for kinematic analysis, identifying critical zones of failure.

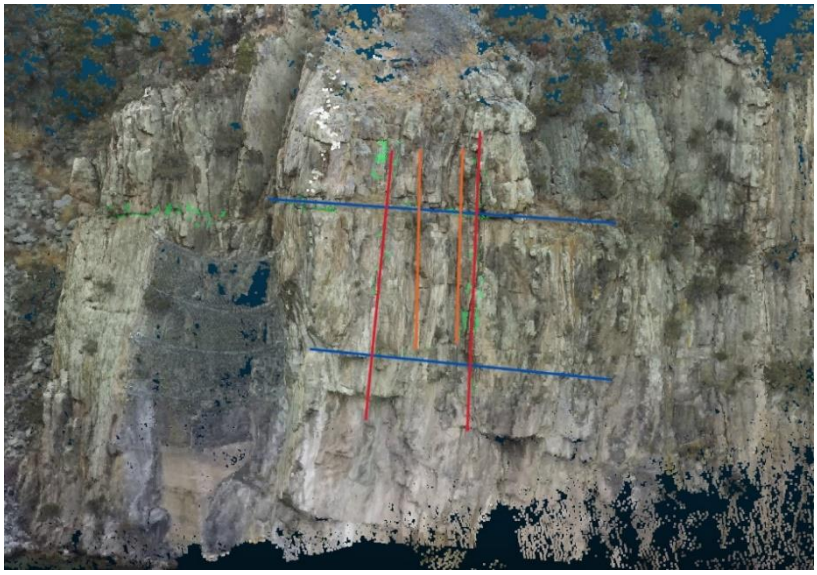

Figure 16: CloudCompare analysis with three joint sets identified (red, blue, and green lines)

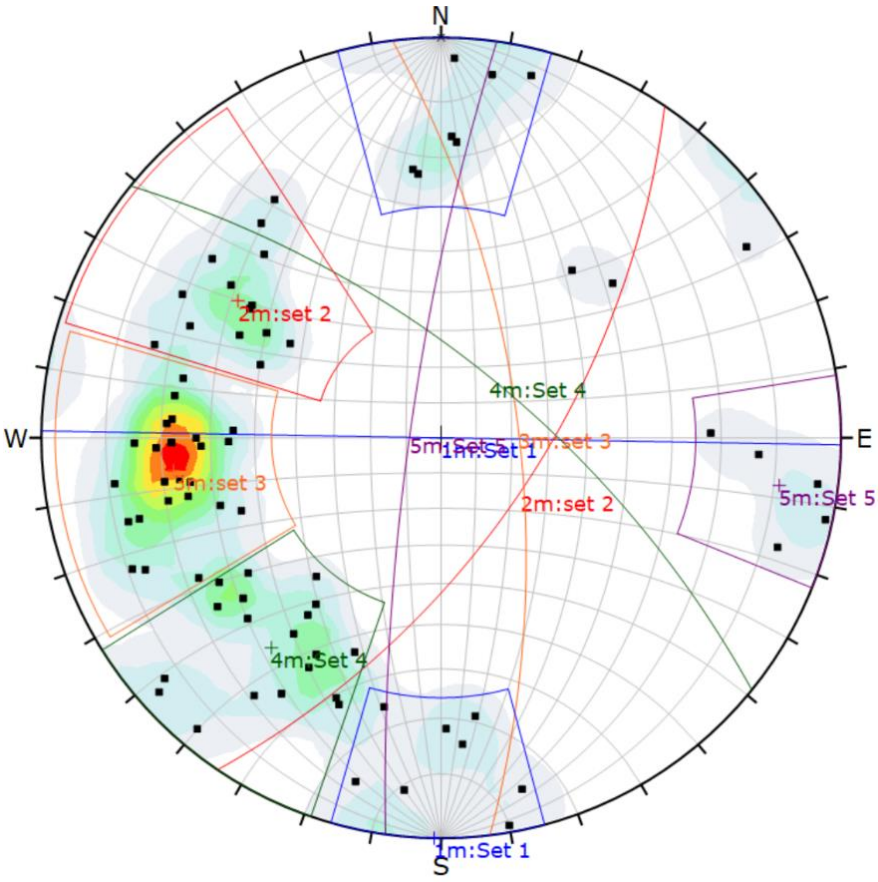

Figure 17: Dips software stereonet, representing five joint sets identified at the site

Table 4: The average dip and dip directions of five joint sets shown in Figure 17. along with symbols for pole vectors, mean set planes and the mean dip and dip directions shown in the figure.

Symbol	Feature
■	Pole Vectors

	Color	Dip	Dip Direction	Label
Mean Set Planes				
1m		90	1	Set 1
2m		63	124	set 2
3m		68	83	set 3
4m		68	39	Set 4
5m		81	278	Set 5

Plot Mode	Pole Vectors
Vector Count	81 (81 Entries)
Hemisphere	Lower
Projection	Equal Angle

5. Engineering Analysis of the Rock Mass

Two types of engineering analyses were performed for this project. Kinematic analysis addresses large-scale slope stability concerns by looking at the potential modes of failure created by the joints in a rock mass. A kinematic analysis was generated using data collected from the Madison Dam site and is described in Section 5.1. For this analysis, Rocscience Dips software was used to generate failure mode results based on dip and dip direction data gathered from the manual flight (rock face) model. A finite element analysis using a discrete fracture network was also performed using Rocscience RS3 software to evaluate potential displacements of the blocks.

5.1. Kinematic Analysis

A kinematic analysis is performed to identify potential failure modes of a rock mass. To perform this analysis at the Madison Dam, drone imagery was processed to collect joint set data. The joint set data generated from the Rocscience Dips software along with 81 joint orientation data points from the CloudCompare software were used to perform a series of kinematic analyses. The potential failure modes include:

- Plane Sliding
- Wedge Sliding
- Flexural Toppling
- Direct Toppling

Running the analysis in the Rocscience Dips software involves using the kinematic analysis tool in the analysis tab (rocsciencesupport.com). The analysis results show all of the potential failure modes created by the joint set data. To perform the analyses, the slope angle and direction must be specified. For this project, the slope angle was set to 90 degrees because of the near vertical nature of the rock mass. The compass orientation of the rock face was determined by using Google Earth. This allowed for an estimated angle from North to determine an adequate orientation. The orientation of the rock mass was determined to be N20E. The (external) joint

friction angle generated from the series of tilt tests (29°) was also used in this analysis. The results provide a "percentage" value that can be interpreted as the "probability of failure" for the failure modes. The following sections provide further details for each of the four failure modes.

"Plane Sliding with No Limits" This analysis calculates the number of poles in the critical zone that are not safe by the joint friction angle, which is plotted as the circle around the center of the diagram (https://www.rocscience.com/help/dips/documentation/kinematic-analysis/planar-sliding). In Figure 18, the critical zone has a light red fill. The "no limits" option means that the critical zone spans half of the stereonet rather than a reduced region which would be a less conservative analysis. The results show that even if the friction angle was higher, the majority of the planes would still fail due to sliding. Out of the 81 data points, 65 are found in the critical zone. Figure 18 also shows that sets 2, 3 and 4 have 100% probability of failure due to plane sliding.

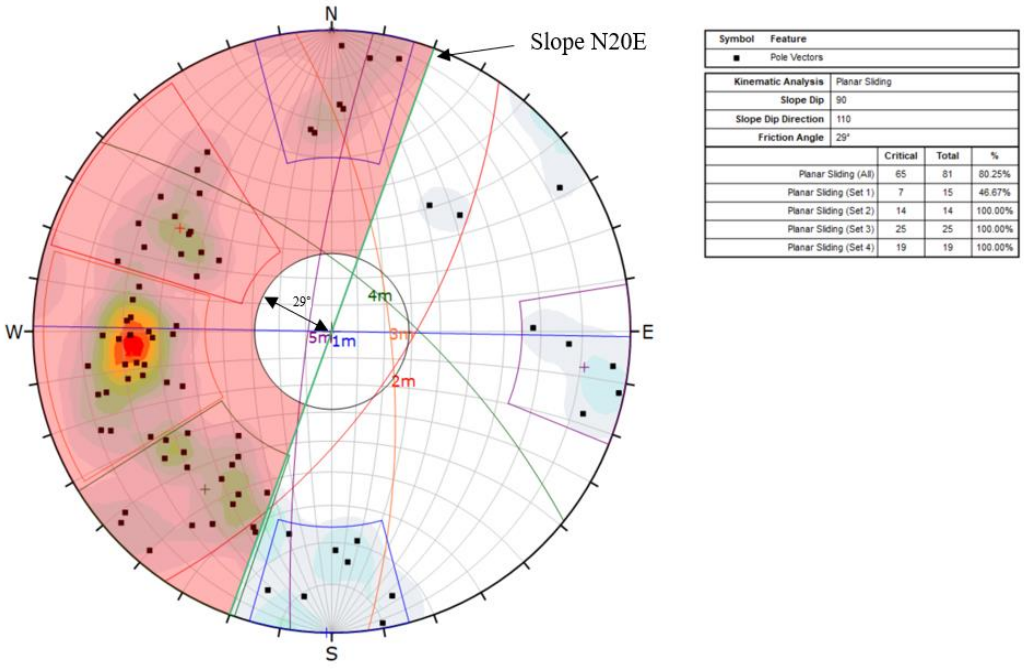

Figure 18: Plane sliding with no limits analysis plot. The area with light red fill is the critical zone. Poles within this zone are expected to fail by plane sliding.

When two joint planes intersect, they can form a wedge which can slide out of the slope. Since wedges can slide along the line of intersection of two planes, the "**Wedge Sliding"** analysis (https://www.rocscience.com/help/dips/documentation/kinematic-analysis/wedge-sliding) is based on the analysis of intersections which are plotted as small red triangles. The primary critical zone (light red shade) represents wedges that satisfy both friction angle and kinematic conditions for sliding on both planes. The secondary critical zone (yellow shade) for Wedge Sliding is the area between the slope plane and a plane inclined at the friction angle, indicating sliding on one side of the wedge. Figure 19 shows the wedge sliding results for the site. In this situation, 74% of the intersections could fail by wedge sliding.

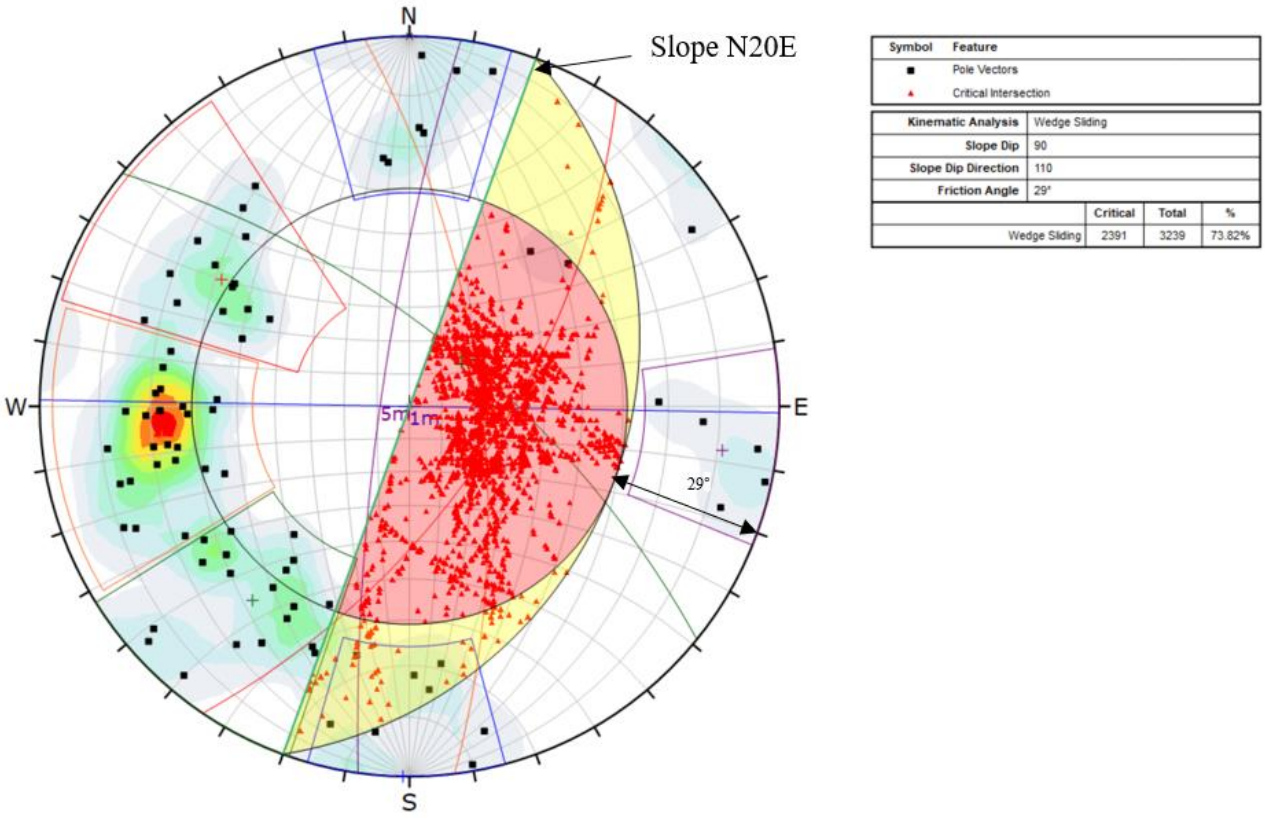

Figure 19: Wedge sliding results. The critical zone has light red fill. Triangles in the critical zone indicate wedge failure. Intersections plotted in the two yellow zones always represent wedges which slide on one joint plane. The intersections in both areas are inclined less than the friction angle where sliding can still take place on a single joint set.

"Flexural Toppling" (https://www.rocscience.com/help/dips/documentation/kinematic-analysis/flexural-toppling) failure is one of the specific modes of toppling failure which occurs due to bending stresses. This type of toppling describes a rock mass that contains a set of parallel discontinuities with a very steep dip angle, like books on a bookshelf. For this analysis, a slip limit is added in order to define a reduced critical zone that only captures the poles in set number five. The results, shown in Figure 20, suggest that only 6% of the planes (and only those associated with set #5) would fail due to flexural toppling.

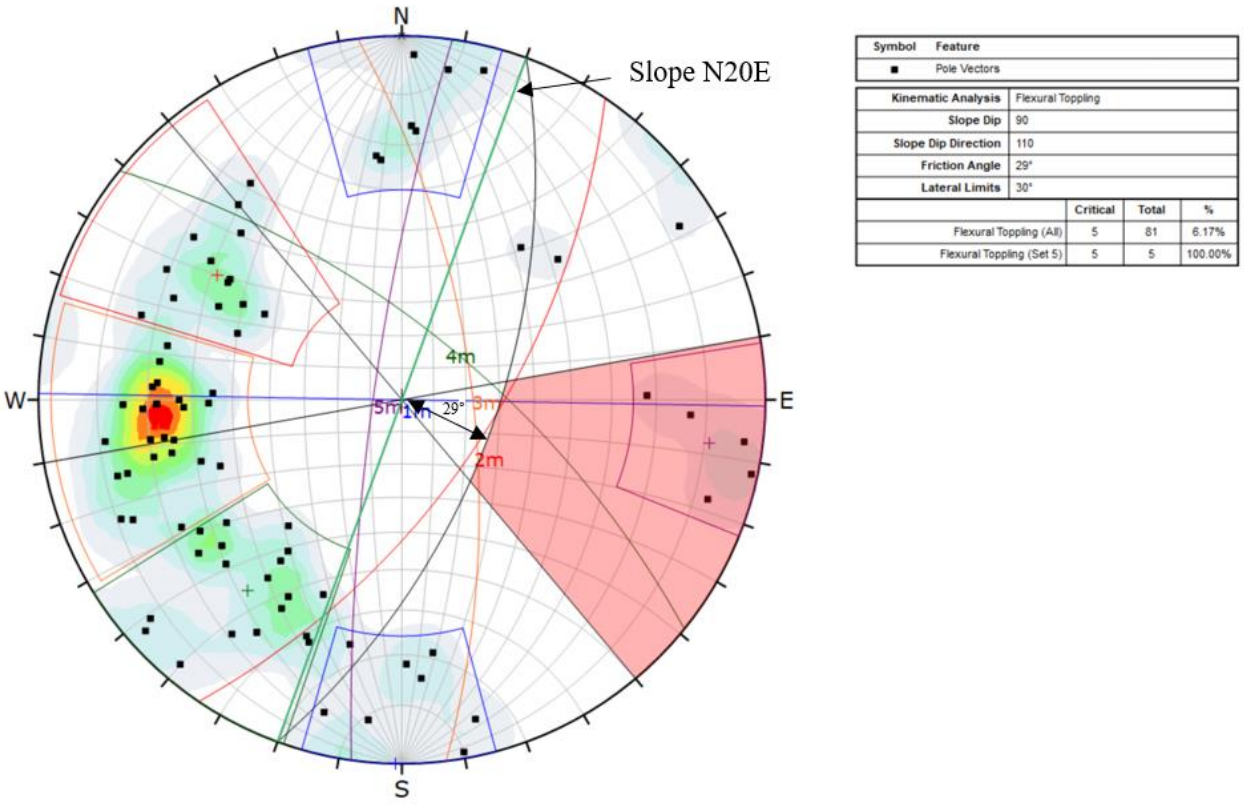

Figure 20: Results of the flexural toppling analysis. Poles in the red critical zone indicate potential flexural toppling failures.

“Direct Toppling” (https://www.rocscience.com/help/dips/documentation/kinematic-analysis/direct-toppling) failure mode is based on in intersection of joint sets meaning that it is focused on wedge-shaped blocks. The critical zone (light red shade) represents configurations in which intersections based on planes create wedges that can fail by direct toppling. Intersections (red triangles) which fall in the critical zone region represent the risk of formation of toppling blocks. Usually, lateral limits are set to narrow the region of failure but in this case, a wide lateral limit was used, which provides a more conservative result. Overall, of the five joint sets present at this site, sets 1-3 have a 100% potential for direct toppling failure and set 4 has an 80% potential for direct toppling. This type of toppling analysis also includes oblique toppling intersections: when the intersections approach vertical toppling in a direction outside the lateral limits is possible. The analysis suggests that there is little to no oblique toppling predicted for this site with only 12 of the 3239 (0.37%) wedges in the critical region for oblique toppling (red triangles inside the 29° friction cone but outside of the red critical zone). Figure 21 shows the results of the direct toppling analysis.

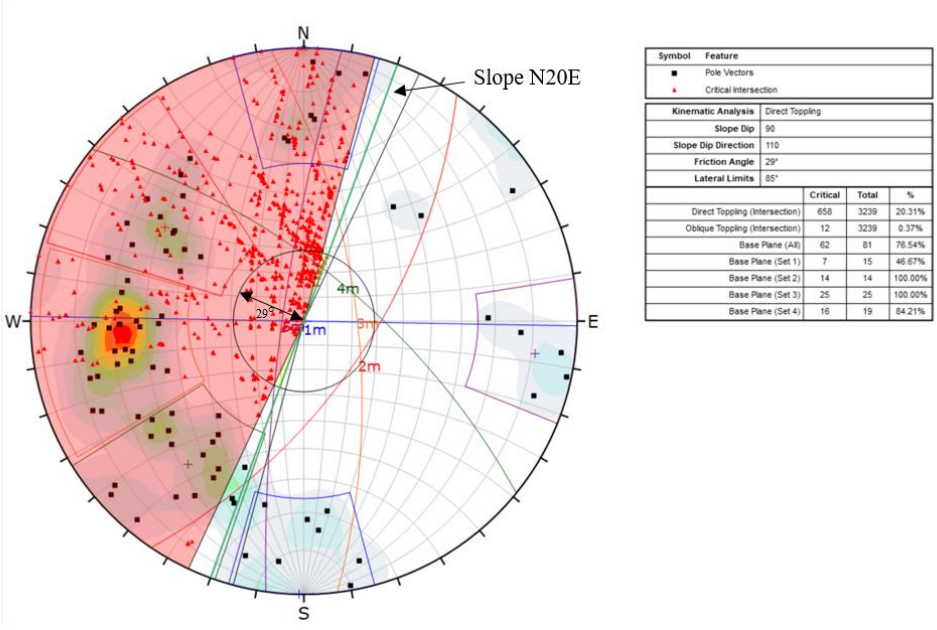

Symbol	Feature
■	Pole Vectors
▲	Critical Intersection

Kinematic Analysis	Direct Toppling
Slope Dip	90
Slope Dip Direction	110
Friction Angle	29°
Lateral Limits	85°

	Critical	Total	%
Direct Toppling (Intersection)	658	3239	20.31%
Oblique Toppling (Intersection)	12	3239	0.37%
Base Plane (All)	62	81	76.54%
Base Plane (Set 1)	7	15	46.67%
Base Plane (Set 2)	14	14	100.00%
Base Plane (Set 3)	25	25	100.00%
Base Plane (Set 4)	16	19	84.21%

Figure 21: Direct toppling results. The critical zone is the light red fill. Triangles in the critical zone indicate wedge-block toppling failure.

This set of analyses shows results of possible rock mass failure scenarios. For this site all the modes of failure are possible but some more than others. The plane sliding and wedge sliding show to have the greatest affect on the rock mass stability. The joint sets also show differences when analyzing different types of failure modes. For example, Joint Set #4 has a 100% probability of failing due to plane sliding, but only a 24% probability of failing due to direct toppling. This is mostly controlled by the orientation of the joint set relative to the slope face, so the results are expected to vary between the different data sets. Table 3 shows the results generated form the kinematic analysis in the Rocscience Dips software.

Table 3: Results showing failure mode probability percentages for each set in all four failure modes analyzed

Failure Mode	All Sets %	Set 1 %	Set 2 %	Set 3 %	Set 4 %	Set 5 %
Plane Sliding	80	47	100	100	100	N/A
Wedge Sliding	74	N/A	N/A	N/A	N/A	N/A
Flexural Toppling	6	N/A	N/A	N/A	N/A	100
Direct Toppling	20	47	100	100	84	N/A

5.2. RS3 Discrete Fracture Network

The finite element method is commonly used in geotechnical engineering to make predictions of deformations and stress conditions that could cause failure. RS3 by Rocscience is a 3D Finite Element Analysis software with an option for fully automated shear strength reduction method for advanced analysis of complex models. While the finite element method was originally intended for solid materials, this study involves a fractured rock mass, so the discrete fracture network (DFN) approach was utilized in RS3 to allow analysis of rock block displacements. The DFN approach for modeling fractured rock masses (https://www.rocscience.com/help/rs3/documentation/geology-excavation/materials/discrete-fracture-networks-dfns) uses explicit representations of fractures forming a network. The joint sets identified in CloudCompare from the point cloud generated in Pix4D mapper were used to

create a discrete fracture network. To characterize the intact rock blocks in RS3, the strength properties from the multistage triaxial test were used. When performing the DFN analysis in RS3, these are the basic steps performed to generate results:

1. import the geometry (point cloud)
2. add an external boundary around the geometry
3. define material properties
4. assign DFN and add joint properties
5. merge the DFN with the geometry
6. add restraints (automatic boundary conditions) to the profile
7. discretize and generate a mesh onto the profile
8. run the model

After these steps are completed, the user can manipulate the results by utilizing the post-processing module in RS3. Figure 22 shows the external boundary and point cloud uploaded into RS3 software.

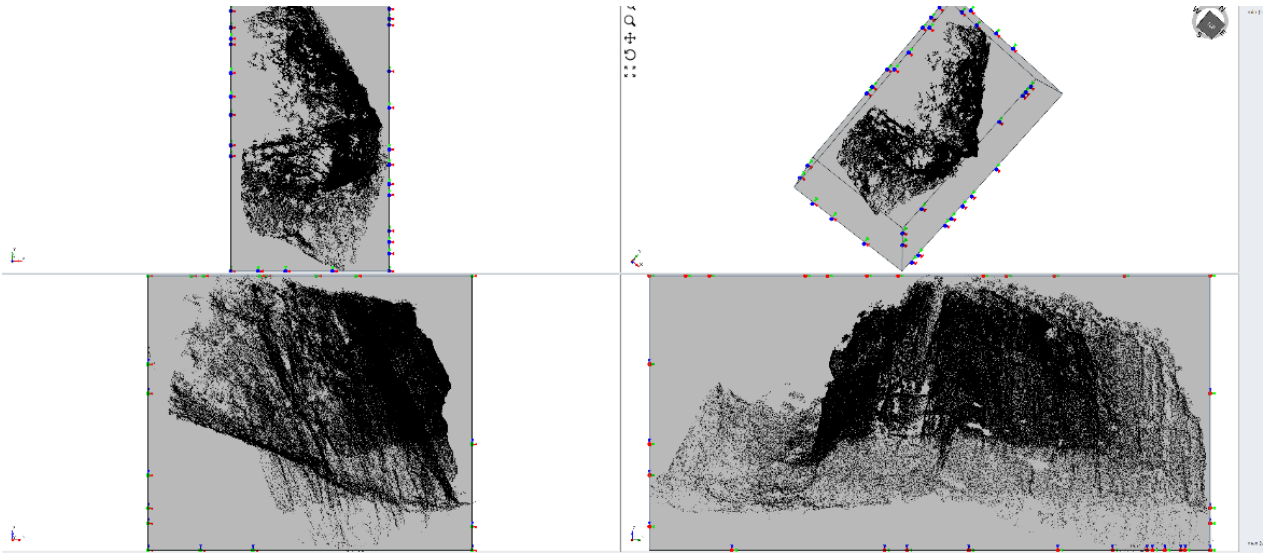

Figure 22: Initial model with external boundary

In the post-processing module, two profiles were generated: strength factor and relative shear displacement. The strength factor option plots the contours of strength factor around the geometry. This is calculated by the induced stress at every point in the mesh and is considered a 3-dimensional result. Figure 23 shows the results from the strength factor calculations. The four diagrams correspond to views from the top, side, and front, and a perspective view. The relative

shear displacement represents which areas are most likely to have a shearing failure. The red areas for strength factor results are -1.0 to 9.0 and the blue area ranges from 79.8-100.0. In this case, the red zones are considered zones that have a possibility of failing. Sections where joints run through the profile show fluctuation in strength factor. The joints appear to have a lower strength factor near intersections. Figures 24, 25, and 26 display the shear displacement of the individual joint sets. In these figures, the diagram on the left is a view looking straight down from the top of the rock mass, and the diagram on the right is a view of looking at the front of the rock mass. The areas showing light green define the slope as safe and the areas of red and dark orange show the slope to have a probability of failure.

The results from the finite element DFN analyses appear to correspond well with field observations. The strength factor shows to be the lowest along the edge of the rock face and along joints especially around the intersections. The shear displacement results appear to have the highest shear displacement along the steepest portion of the rock mass.

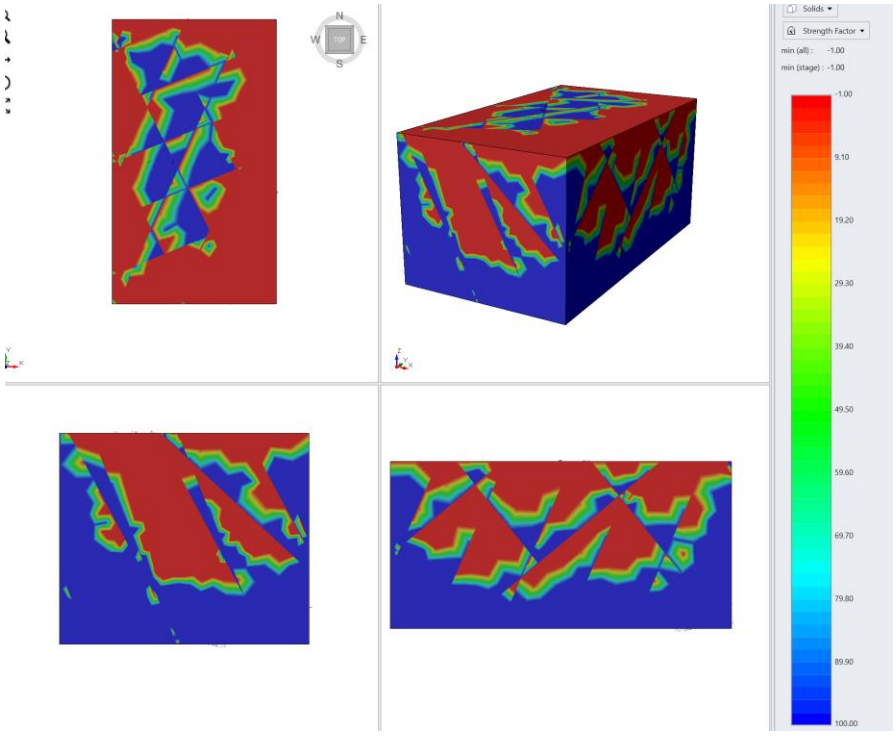

Figure 23. Strength factor including all 3 joint sets

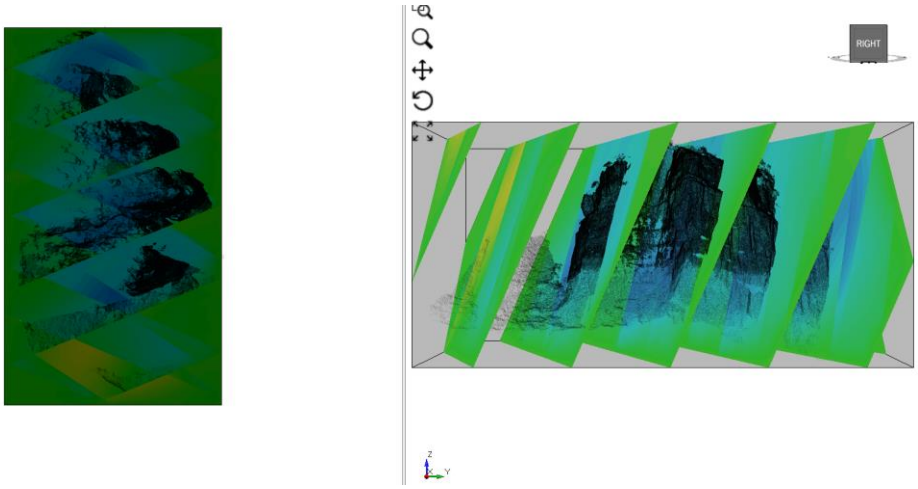

Figure 24. Shear displacements calculated for the joint set with dip 64 and dip direction 158. The left bock shows the top view and the right bock shows the front view.

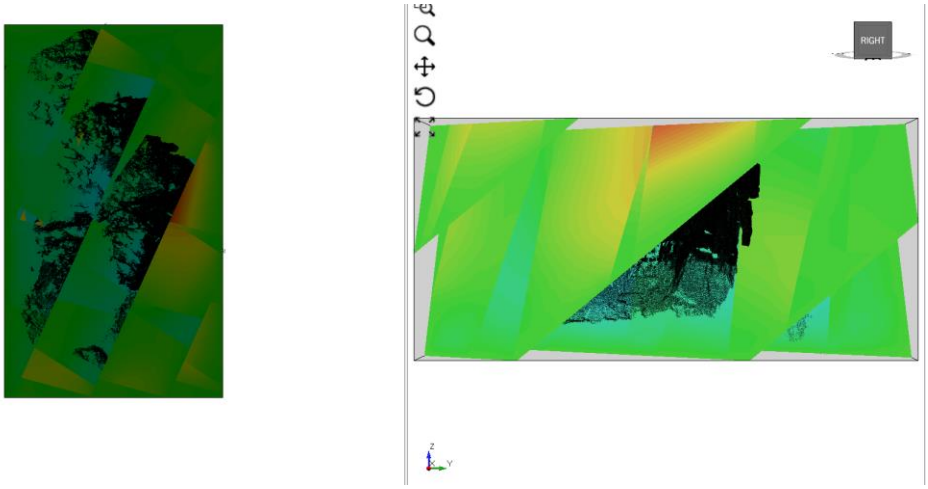

Figure 25: Shear displacements calculated for the joint set with dip 68 and dip direction 114. The left bock shows the top view and the right bock shows the front view.

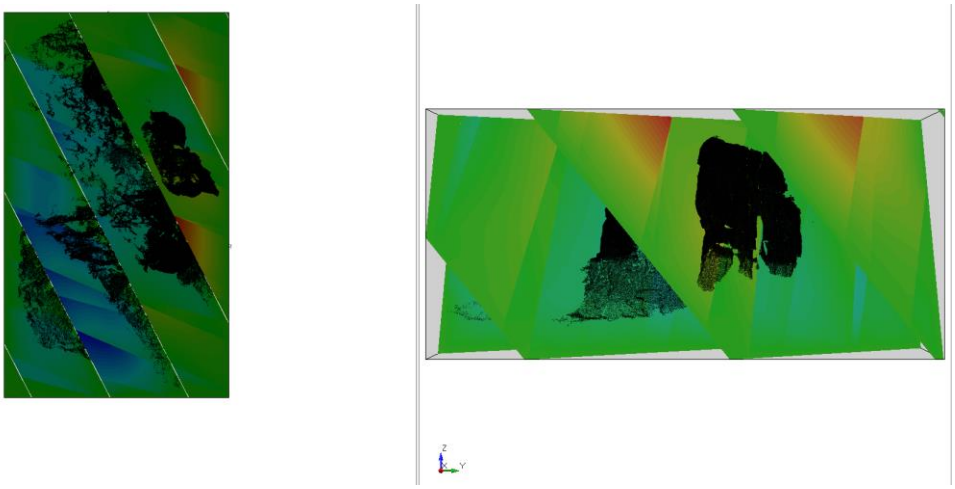

Figure 26: Shear displacements calculated for the joint set with dip 70 and dip direction 063. The left bock shows the top view and the right bock shows the front view.

6. Conclusions and Recommendations

For this project, rock mass strength characteristics were determined through laboratory tests and rock mass failure modes were identified using drone imagery data. The engineering analyses involved kinematic analysis and finite element modeling using the manual flight data modeled in Pix4D mapper. The analyses results predict plane sliding, wedge sliding, flexural toppling, and direct toppling modes of failure may be present.

To ensure that people working at the dam and the structure are safe from falling rocks some safety solutions could be installed. This may include extending the existing mesh at the site to cover the potentially hazardous rock, inserting rock bolts into blocks that may pose a risk of falling, constructing a caged breezeway to deflect smaller and medium-sized rocks from landing on dam workers, and possibly removing blocks that may be prone to falling.

For future investigations involving data collection using drones, there are a few improvements that can be made. Having a drone that can perform vertical autonomous flights to capture high-quality photogrammetric data would improve the accuracy of models created even without GCPs. This would allow the collection of images that have a certain overlap without having to estimate the overlap when extracting from video and would improve the modeling of the near vertical rock face. Placing surveyed ground control points along the rock mass face will improve the model's accuracy when processing the images and provide more confidence in joint set orientations. Collecting more rock samples and coring the rock at different angles along the layering could provide a more comprehensive set of rock strength property results and would potentially improve the finite element models. With the growing technological advances of drone there is a great potential to enhance rock mass analysis in the engineering community.

References Cited

Dams in Montana, dnrc.mt.gov/_docs/water/Dam_Safety/PUBLICATIONS/Dams-in-Montana-12-28-2018.pdf. Accessed 1 June 2024.

Goodman, R.E. (1989). Engineering Geology: Rocks in Engineering Construction. John Wiley & Sons Ltd., New York.

Pinckney, Darrell, "Resource potential of the Bear Trap Canyon Instant Study Area, Madison County, Montana." *UNITED STATES DEPARTMENT OF THE INTERIOR GEOLOGICAL SURVEY*, 1980.

Kim, M. M., & Ko, H. Y. (1979). Multistage triaxial testing of rocks. *Geotechnical Testing Journal*, *2*(2), 98-105.

"Kinematic Analysis Overview." *Dips Documentation | Kinematic Analysis Overview*, www.rocscience.com/help/dips/documentation/kinematic-analysis/direct-toppling#page-content-1. Accessed 27 Apr. 2024.

"Missouri-Madison Hydroelectric Project 2188: Northwestern Energy." *Default*, www.northwesternenergy.com/clean-energy/our-environmental-projects/missouri-madison-hydro-project-2188. Accessed 9 Apr. 2024.

"NGMDB Product Description Page." *Ngmdb.usgs.gov*, ngmdb.usgs.gov/Prodesc/proddesc_96020.htm. Accessed 29 May 2024.

Niedzielski, Tomasz. "Applications of Unmanned Aerial Vehicles in Geosciences: Introduction." *Pure and Applied Geophysics*, vol. 175, no. 9, Sept. 2018, pp. 3141–3144, paperity.org/p/158959171/applications-of-unmanned-aerial-vehicles-in-geosciences-introduction, https://doi.org/10.1007/s00024-018-1992-9.

Pix4D (2024) "Software Manual > Table View - PIX4Dmapper." *Support.pix4d.com*, support.pix4d.com/hc/en-us/articles/202557969. Accessed 21 May 2024.

Quality Report Help - Pix4dmapper, support.pix4d.com/hc/en-us/articles/202558689-Quality-Report-Help-PIX4Dmapper. Accessed 10 Apr. 2024.

Rocscience (2024). Dips User Guide, www.rocscience.com/help/dips/overview. Accessed 2 May 2024.

Rocscience (2024). Dips Documentation | Kinematic Analysis, www.rocscience.com/help/dips/documentation/kinematic-analysis. Accessed 2 May 2024.

"Software Manual > Table View - PIX4Dmapper." *Support.pix4d.com*, support.pix4d.com/hc/en-us/articles/202557969. Accessed 21 May 2024.

Williams, Brian J., and NTL Engineering & Geosciense, Inc. Geotechnical Engineering Report, Madison Dam Rockfall Remediation, Madison County, Montana. NTL Terracon, 20 Jan. 2011.

Appendix A: Methodology Flowchart and Pix4D Quality Report

UAV Data and Rock Sample Collection

Built 3D Models

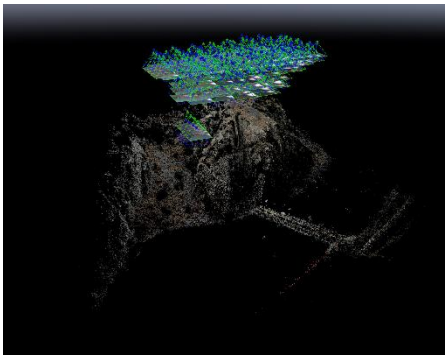

Rock Strength Testing Using Samples From Project Area

Used Models to Collect Dip and Dip Direction of Joint Sets

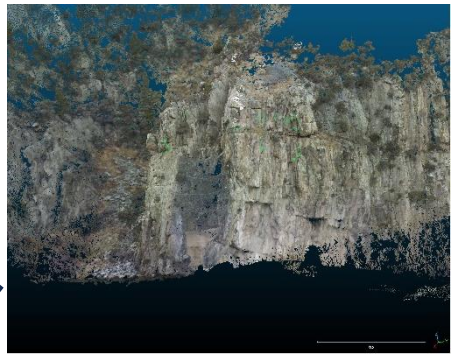

Stability Analysis performed using Dip and Dip Direction Measurements and Rock Strength Results

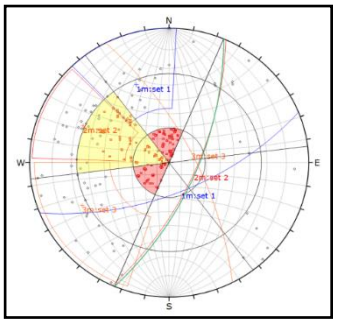

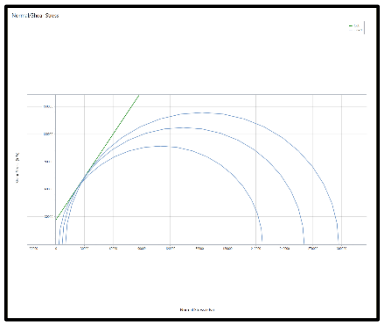

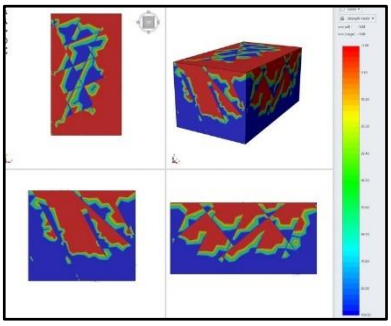

Quality Report

Generated with Pix4Dmapper version 4.6.4

Important: Click on the different icons for:

Help to analyze the results in the Quality Report

Additional information about the sections

Click here for additional tips to analyze the Quality Report

Summary

Project	Original Flight
Processed	2024-03-29 09:39:49
Camera Model Name(s)	Anafi_4.0_4608x3456 (RGB)
Average Ground Sampling Distance (GSD)	1.70 cm / 0.67 in
Area Covered	undefined

Quality Check

Images	median of 44639 keypoints per image	✓
Dataset	207 out of 207 images calibrated (100%), all images enabled	✓
Camera Optimization	1% relative difference between initial and optimized internal camera parameters	✓
Matching	median of 16346.4 matches per calibrated image	✓
Georeferencing	no, no 3D GCP	⚠

Preview

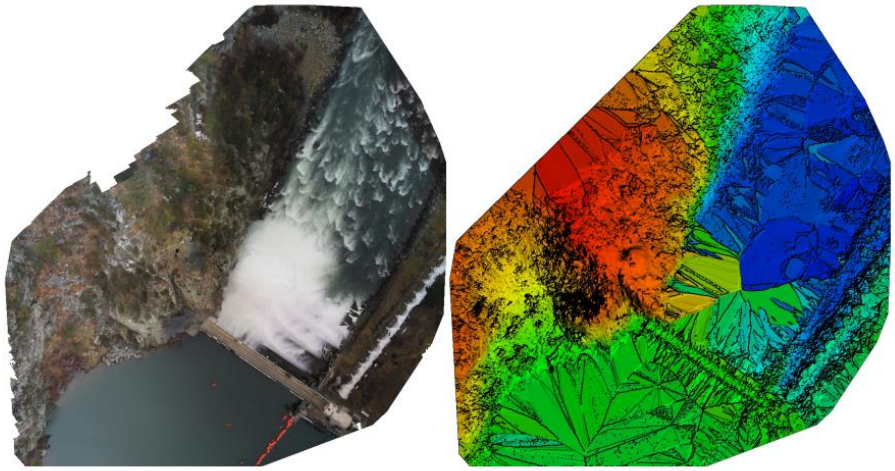

Figure 1: Orthomosaic and the corresponding sparse Digital Surface Model (DSM) before densification.

Calibration Details

Number of Calibrated Images	207 out of 207
Number of Geolocated Images	207 out of 207

Initial Image Positions

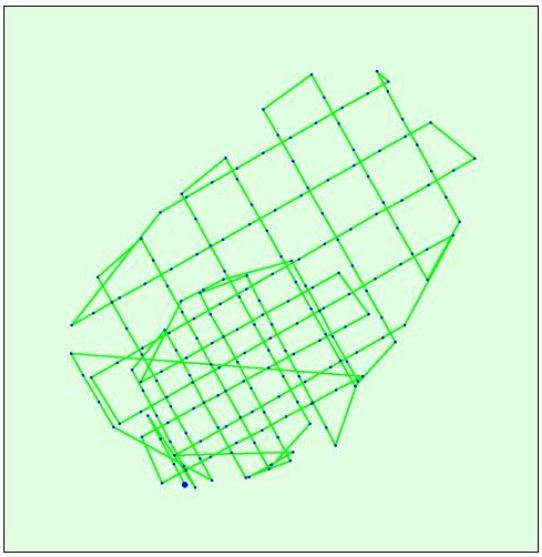

Figure 2: Top view of the initial image position. The green line follows the position of the images in time starting from the large blue dot.

Computed Image/GCPs/Manual Tie Points Positions

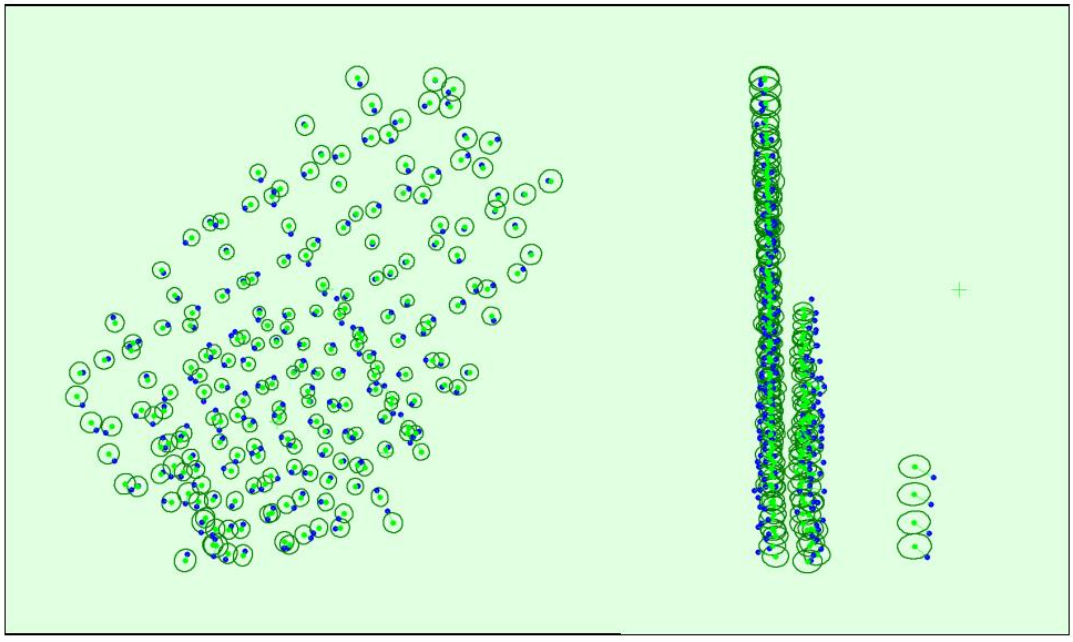

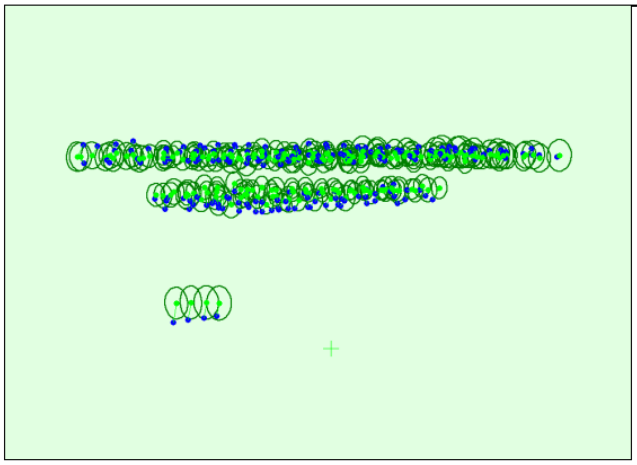

Uncertainty ellipses 50x magnified

Figure 3: Offset between initial (blue dots) and computed (green dots) image positions as well as the offset between the GCPs initial positions (blue crosses) and their computed positions (green crosses) in the top-view (XY plane), front-view (XZ plane), and side-view (YZ plane). Dark green ellipses indicate the absolute position uncertainty of the bundle block adjustment result.

Absolute camera position and orientation uncertainties

	X [ft]	Y [ft]	Z [ft]	Omega [degree]	Phi [degree]	Kappa [degree]
Mean	0.081	0.082	0.111	0.059	0.049	0.040
Sigma	0.014	0.014	0.017	0.000	0.000	0.000

Overlap

Figure 4: Number of overlapping images computed for each pixel of the orthomosaic.
Red and yellow areas indicate low overlap for which poor results may be generated. Green areas indicate an overlap of over 5 images for every pixel. Good quality results will be generated as long as the number of keypoint matches is also sufficient for these areas (see Figure 5 for keypoint matches).

Bundle Block Adjustment Details

Number of 2D Keypoint Observations for Bundle Block Adjustment	3493211
Number of 3D Points for Bundle Block Adjustment	1118975
Mean Reprojection Error [pixels]	0.254

Internal Camera Parameters

Anafi_4.0_4608x3456 (RGB). Sensor Dimensions: 6.194 [mm] x 4.646 [mm]

EXIF ID: AnafiUSA_4.0_4608x3456

	Focal Length	Principal Point x	Principal Point y	R1	R2	R3	T1	T2
Initial Values	2993.870 [pixel] 4.024 [mm]	2306.380 [pixel] 3.100 [mm]	1710.170 [pixel] 2.299 [mm]	0.003	0.001	-0.002	-0.002	0.001
Optimized Values	3023.912 [pixel] 4.065 [mm]	2297.275 [pixel] 3.088 [mm]	1749.263 [pixel] 2.351 [mm]	-0.000	0.004	-0.003	0.004	0.000
Uncertainties (Sigma)	4.619 [pixel] 0.006 [mm]	0.102 [pixel] 0.000 [mm]	0.052 [pixel] 0.000 [mm]	0.000	0.000	0.000	0.000	0.000

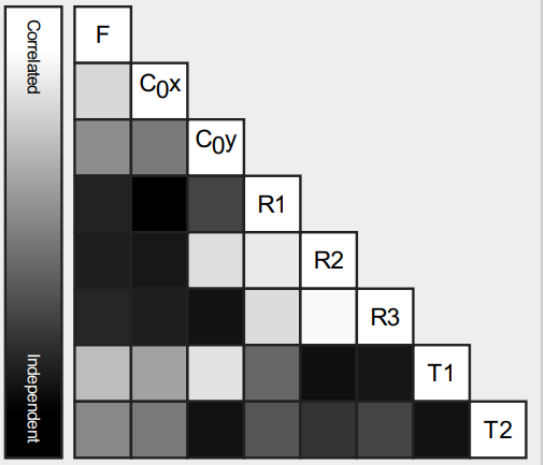

The correlation between camera internal parameters determined by the bundle adjustment. White indicates a full correlation between the parameters, ie. any change in one can be fully compensated by the other. Black indicates that the parameter is completely independent, and is not affected by other parameters.

The number of Automatic Tie Points (ATPs) per pixel, averaged over all images of the camera model, is color coded between black and white. White indicates that, on average, more than 16 ATPs have been extracted at the pixel location. Black indicates that, on average, 0 ATPs have been extracted at the pixel location. Click on the image to the see the average direction and magnitude of the re-projection error for each pixel. Note that the vectors are scaled for better visualization. The scale bar indicates the magnitude of 1 pixel error.

2D Keypoints Table

	Number of 2D Keypoints per Image	Number of Matched 2D Keypoints per Image
Median	44639	16346
Min	24305	4179
Max	76581	33215
Mean	46383	16875

3D Points from 2D Keypoint Matches

	Number of 3D Points Observed

In 2 Images	737940
In 3 Images	181414
In 4 Images	75698
In 5 Images	38547
In 6 Images	22556
In 7 Images	14422
In 8 Images	9928
In 9 Images	7038
In 10 Images	5180
In 11 Images	3984
In 12 Images	3091
In 13 Images	2520
In 14 Images	1994
In 15 Images	1675
In 16 Images	1413
In 17 Images	1140
In 18 Images	956
In 19 Images	859
In 20 Images	758
In 21 Images	657
In 22 Images	592
In 23 Images	545
In 24 Images	433
In 25 Images	418
In 26 Images	349
In 27 Images	352
In 28 Images	288
In 29 Images	248
In 30 Images	240
In 31 Images	215
In 32 Images	204
In 33 Images	202
In 34 Images	182
In 35 Images	168
In 36 Images	154
In 37 Images	127
In 38 Images	126
In 39 Images	134
In 40 Images	123
In 41 Images	107
In 42 Images	87
In 43 Images	92
In 44 Images	89
In 45 Images	82
In 46 Images	77
In 47 Images	86
In 48 Images	61
In 49 Images	60
In 50 Images	58
In 51 Images	46
In 52 Images	45
In 53 Images	64
In 54 Images	54
In 55 Images	51
In 56 Images	50
In 57 Images	37
In 58 Images	31
In 59 Images	41
In 60 Images	37

In 61 Images	24
In 62 Images	44
In 63 Images	22
In 64 Images	31
In 65 Images	31
In 66 Images	28
In 67 Images	23
In 68 Images	22
In 69 Images	33
In 70 Images	25
In 71 Images	31
In 72 Images	19
In 73 Images	16
In 74 Images	16
In 75 Images	15
In 76 Images	17
In 77 Images	26
In 78 Images	18
In 79 Images	18
In 80 Images	14
In 81 Images	13
In 82 Images	25
In 83 Images	15
In 84 Images	22
In 85 Images	13
In 86 Images	13
In 87 Images	9
In 88 Images	8
In 89 Images	5
In 90 Images	14
In 91 Images	10
In 92 Images	11
In 93 Images	15
In 94 Images	14
In 95 Images	14
In 96 Images	6
In 97 Images	8
In 98 Images	13
In 99 Images	7
In 100 Images	8
In 101 Images	6
In 102 Images	3
In 103 Images	6
In 104 Images	9
In 105 Images	5
In 106 Images	2
In 107 Images	6
In 108 Images	3
In 109 Images	3
In 110 Images	4
In 111 Images	8
In 112 Images	5
In 113 Images	3
In 114 Images	7
In 115 Images	6
In 116 Images	4
In 117 Images	9
In 118 Images	3
In 119 Images	2

In 120 Images	6
In 121 Images	3
In 122 Images	5
In 123 Images	2
In 124 Images	2
In 126 Images	4
In 127 Images	1
In 128 Images	4
In 130 Images	1
In 131 Images	4
In 133 Images	2
In 136 Images	1
In 138 Images	1
In 139 Images	1
In 140 Images	1
In 142 Images	1
In 143 Images	1

2D Keypoint Matches

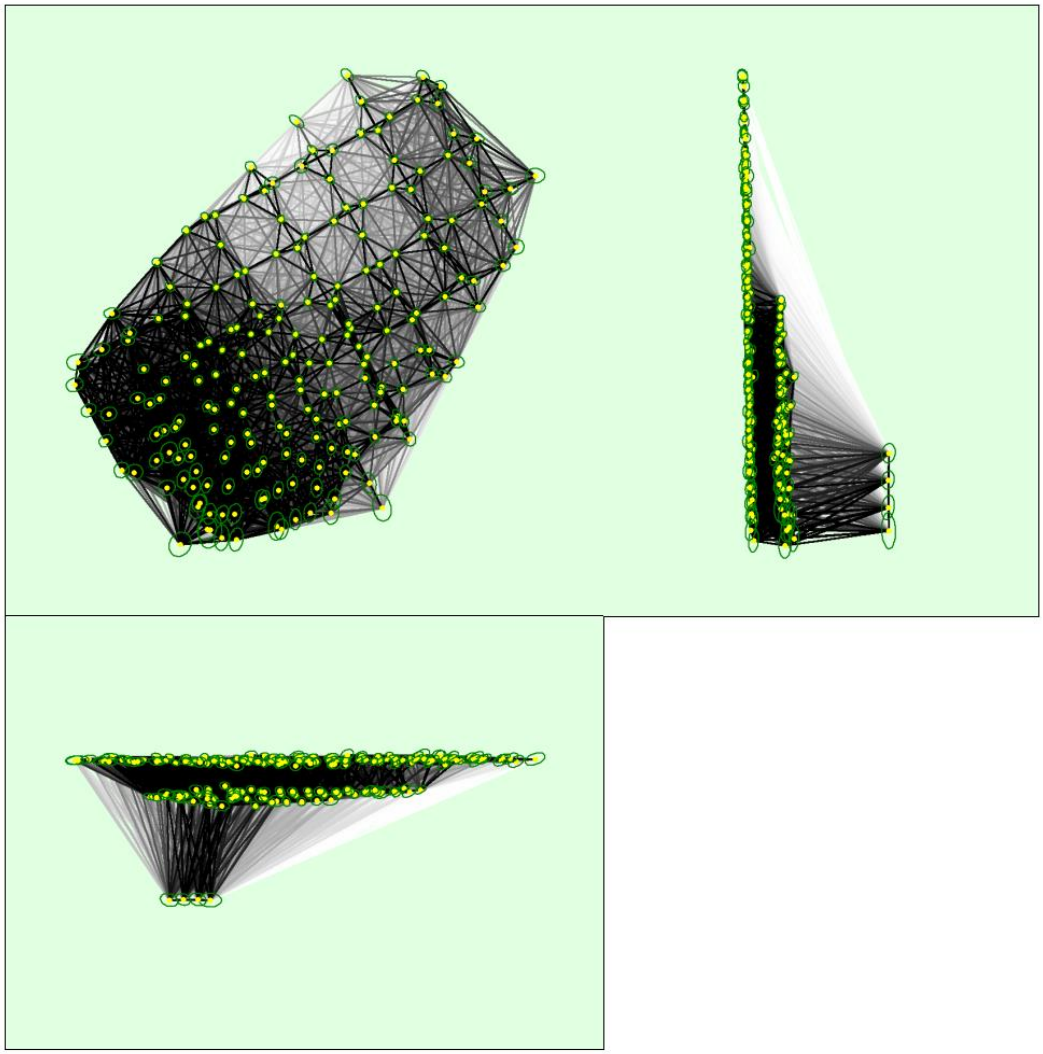

Uncertainty ellipses 500x magnified

Figure 5: Computed image positions with links between matched images. The darkness of the links indicates the number of matched 2D keypoints between the images. Bright links indicate weak links and require manual tie points or more images. Dark green ellipses indicate the relative camera position uncertainty of the bundle block adjustment result.

Relative camera position and orientation uncertainties

	X [ft]	Y [ft]	Z [ft]	Omega [degree]	Phi [degree]	Kappa [degree]
Mean	0.006	0.006	0.004	0.003	0.003	0.002
Sigma	0.002	0.002	0.001	0.001	0.001	0.000

Manual Tie Points

MTP Name	Projection Error [pixel]	Verified/Marked
mtp1	2.004	82 / 83
mtp2	1.218	98 / 98
mtp3	0.850	123 / 124

Projection errors for manual tie points.The last column counts the number of images where the manual tie point has been automatically verified vs. manually marked.

Geolocation Details

Absolute Geolocation Variance

Min Error [ft]	Max Error [ft]	Geolocation Error X [%]	Geolocation Error Y [%]	Geolocation Error Z [%]
-	-8.15	0.00	0.00	0.97
-8.15	-6.52	0.00	0.00	4.83
-6.52	-4.89	0.00	2.42	8.70
-4.89	-3.26	6.28	7.25	9.66
-3.26	-1.63	22.22	19.81	12.56
-1.63	0.00	28.02	19.81	18.84
0.00	1.63	26.09	21.74	16.91
1.63	3.26	15.94	22.71	10.14
3.26	4.89	1.45	2.90	9.66
4.89	6.52	0.00	2.42	5.31
6.52	8.15	0.00	0.97	1.93
8.15	-	0.00	0.00	0.48
Mean [ft]		-0.296800	-0.128934	-0.534797
Sigma [ft]		1.995608	2.507575	3.755105
RMS Error [ft]		0.017559	0.510888	0.792997

Min Error and Max Error represent geolocation error intervals between -1.5 and 1.5 times the maximum accuracy of all the images. Columns X, Y, Z show the percentage of images with geolocation errors within the predefined error intervals. The geolocation error is the difference between the initial and computed image positions. Note that the image geolocation errors do not correspond to the accuracy of the observed 3D points.

Relative Geolocation Variance

Relative Geolocation Error	Images X [%]	Images Y [%]	Images Z [%]
[-1.00, 1.00]	82.13	75.36	64.25
[-2.00, 2.00]	100.00	99.03	97.10
[-3.00, 3.00]	100.00	100.00	100.00
Mean of Geolocation Accuracy [ft]	2.897370	2.897370	4.070841

Images X, Y, Z represent the percentage of images with a relative geolocation error in X, Y, Z.

Geolocation Orientational Variance	RMS [degree]
Omega	1.663
Phi	0.697
Kappa	1.850

Geolocation RMS error of the orientation angles given by the difference between the initial and computed image orientation angles.

Initial Processing Details

System Information

Hardware	CPU: Intel(R) Xeon(R) W-2255 CPU @ 3.70GHz RAM: 64GB GPU: NVIDIA RTX A5000 (Driver: 31.0.15.3667)
Operating System	Windows 10 Enterprise, 64-bit

Coordinate Systems

Image Coordinate System	WGS 84 (EGM96 Geoid)
Output Coordinate System	WGS 84 / UTM zone 12N (ft) (EGM96 Geoid)

Processing Options

Detected Template	3D Maps
Keypoints Image Scale	Full, Image Scale: 1
Advanced: Matching Image Pairs	Aerial Grid or Corridor
Advanced: Matching Strategy	Use Geometrically Verified Matching: no
Advanced: Keypoint Extraction	Targeted Number of Keypoints: Automatic
Advanced: Calibration	Calibration Method: Standard Internal Parameters Optimization: All External Parameters Optimization: All Rematch: Auto, yes

Point Cloud Densification details

Processing Options

Image Scale	multiscale, 1/2 (Half image size, Default)
Point Density	Optimal
Minimum Number of Matches	3
3D Textured Mesh Generation	yes
3D Textured Mesh Settings:	Resolution: Medium Resolution (default) Color Balancing: no
LOD	Generated: no
Advanced: 3D Textured Mesh Settings	Sample Density Divider: 1
Advanced: Image Groups	group1
Advanced: Use Processing Area	yes
Advanced: Use Annotations	yes
Time for Point Cloud Densification	23m:11s
Time for Point Cloud Classification	NA
Time for 3D Textured Mesh Generation	04m:39s

Results

Number of Generated Tiles	1
Number of 3D Densified Points	10658870
Average Density (per ft^3)	17.36

DSM, Orthomosaic and Index Details

Processing Options

DSM and Orthomosaic Resolution	1 x GSD (1.7 [cm/pixel])
DSM Filters	Noise Filtering: yes Surface Smoothing: yes, Type: Sharp
Raster DSM	Generated: yes Method: Inverse Distance Weighting Merge Tiles: yes
Orthomosaic	Generated: yes Merge Tiles: yes GeoTIFF Without Transparency: no Google Maps Tiles and KML: no
Time for DSM Generation	03m:32s
Time for Orthomosaic Generation	12m:38s
Time for DTM Generation	00s
Time for Contour Lines Generation	00s
Time for Reflectance Map Generation	00s
Time for Index Map Generation	00s

Appendix B: Tilt Test and Dip/Dip Direction data

Table B1: Tilt test data representing all 50 trials performed and the average external (joint) friction angle

Trial Number	Tilt Angle	Trial Number	Tilt Angle
1	15.4	26	28.5
2	27.8	27	35.5
3	34	28	35.4
4	27.5	29	20.7
5	31.5	30	26.2
6	26.6	31	32.5
7	32.6	32	31.4
8	27.8	33	35
9	31.5	34	30.9
10	26.6	35	31
11	31.8	36	34.6
12	29.2	37	22.9
13	34.9	38	23.8
14	24.5	39	30.9
15	28	40	27.5
16	29.1	41	24.4
17	32.7	42	27.5
18	25.4	43	28.9
19	21.8	44	29.2
20	27.6	45	37.5
21	24.4	46	30.4
22	28	47	32.2
23	35.5	48	37.1
24	33.3	49	30.9
25	34.4	50	31.5

Table B2: Dip and Dip Direction data

Dip	Dip Direction	Joint Set Location
67	81	2
86	194	
72	145	1
54	121	1
59	117	1
60	124	1
70	77	2
69	12	3
52	112	1
56	70	2
62	88	2
76	75	2
84	238	
60	228	
71	88	2
70	140	1
67	103	1
84	347	3
70	353	3
61	55	3
65	136	1
56	218	
48	122	1
60	125	1
78	75	2
65	51	3
64	30	3
67	30	3
70	22	3
79	82	2
80	67	2
67	57	2
85	49	3
78	66	2
68	99	2
60	73	2
75	89	2
63	37	3
74	32	3
71	21	3
67	47	3
58	37	3
65	80	2
50	42	3
55	37	3
75	356	3
87	40	3
73	183	
87	182	
70	60	2
70	81	2
70	53	3
83	06	3
74	182	
85	188	
77	36	3
67	175	
87	48	3
83	14	3
68	174	
60	22	3
72	359	3
89	350	
68	269	
77	237	
89	282	
83	288	
87	277	
69	93	2
68	89	2
66	77	2
68	89	2
56	89	2
68	94	2
63	90	2
55	92	2
69	114	1
72	128	1
66	126	1
74	108	1
73	119	1